Supporting Information

Skin-interfaced microfluidic devices with one-opening chambers and hydrophobic valves for sweat collection and analysis

Yingxue Zhang,[1,2§] Yao Chen,[1§] Jielong Huang,[1] Yangchengyi Liu,[1] Jinfeng Peng,[3] Shangda Chen,[1] Kui Song,[4] Xiaoping Ouyang,[1] Huanyu Cheng,[2*] and Xiufeng Wang,[1,5*]

[1]School of Materials Science and Engineering, Xiangtan University, Xiangtan, Hunan 411105, China

[2]Department of Engineering Science and Mechanics, The Pennsylvania State University, University Park, PA 16802, USA.

[3]School of Mechanical Engineering, Xiangtan University, Xiangtan, Hunan 411105, China

[4]College of Civil Engineering and Mechanics, Xiangtan University, Xiangtan, Hunan 411105, China

[5]Institute of Flexible Electronics Technology of Tsinghua University, Jiaxing, Zhejiang 314006, China

---

Corresponding Author

[*]E-mail: onexf@xtu.edu.cn (X.W.)

[*]E-mail: Huanyu.Cheng@psu.edu (H.C.)

[§]Y.Z. and Y.C. contributed equally to this work.

METHODS

Modeling of One-Opening Chambers with the HV

The bridging channel between the main channel and a collection chamber includes a short microchannel (length of h=80 μm and width of b=500 μm) and two transition channels with a radius of r=300 μm (Figure S6). The centers of the top and bottom transition channels are located at Point A ($x = 0, y = L$) and B ($x = 0, y = L + h$). The geometry of the fluid front in the bridging channel is illustrated in Figure S7a-c, where α is the apparent angle between the tangent to the channel wall and the straight line of the air-liquid interface, θ_A is the constant contact angle at the channel wall, and b_* is the effective channel width. Because $|CD|$ and $|EC|$ are expressed as $x - r\sin\theta_e$ and $L - r\cos\theta_e$, respectively, the effective channel width is solved as $b_* = \sqrt{|CD|^2 + |EC|^2} = \sqrt{(L^2 + r^2) + x^2 - 2r(x\sin\theta_e + L\cos\theta_e)}$. Considering $\beta = \alpha - \theta_A$, the following relationship is obtained:

$$\sin\beta = \frac{|EC|}{b_*}\cos\theta_A - \frac{|CD|}{b_*}\sin\theta_A = \left[(L - r\cos\theta_e)\cos\theta_A - (x - r\sin\theta_e)\sin\theta_A\right]/b_* . \quad \text{(S1)}$$

The perpendicular components of the surface tension to the liquid surface (Figure S7d) can be expressed as

$$\begin{cases} F_b = F_{DU}\sin\beta = 2\sigma h\sin\beta \\ F_h = F_{ED}\cos\theta_A = 2\sigma b_*\cos\theta_A, \end{cases} \quad \text{(S2)}$$

where σ is the surface tension of the liquid and h is the channel height. The pressure across the air-liquid interface in the channel (P_i) is then expressed as

$$P_i = \frac{F_b + F_h}{b_* h} = 2\sigma\left[\frac{\sin\beta}{b_*} + \frac{\cos\theta_A}{h}\right], \quad \text{(S3)}$$

where θ_A remains as a constant. As the capillary pressure difference (ΔP) that drives the liquid advancing front into the chamber is mainly contributed by P_i and the second term in Eq. S3 is independent of the position, the first term (i.e., $P_b = 2\sigma sin\beta/b_*$) in Eq. S3 is then systematically investigated.

Considering the position of advancing front (l and x in Figure 5a), the normalized variables $l^{'} = l/r = \theta_e$ and $x^{'} = x/r$ also denote the location of the air-fluid interface. When the air-liquid interface advances to the 1st segment (i.e., the bottom transition channel, $0 \le l^{'} \le \pi/2$ in Figure S7a), the normalized driving pressure $P_b r/(2\sigma)$ can be written as

$$\frac{P_b}{2\sigma}r = \frac{L^{'}\cos\theta_A - \cos\left(l^{'} + \theta_A\right) - x^{'}\sin\theta_A}{1 + L^{'2} + x^{'2} - 2L^{'}\cos l^{'} - 2x^{'}\sin l^{'}}, 0 \le l^{'} \le \frac{\pi}{2}, \quad \text{(S4a)}$$

where $L^{'}$ is defined as $L^{'} = L/r$. As the air-liquid interface advances the 2nd segment (i.e., the short microchannel, $\pi/2 \le l^{'} \le \pi/2 + 1/4$ in Figure S7b) and the 3rd segment (i.e., the top transition channel, $\pi/2 + 1/4 \le l^{'} \le \pi + 1/4$ in Figure S7d), the normalized driving pressures are obtained as:

$$\frac{P_b}{2\sigma}r = \frac{\left(L^{'} + l^{'} - 0.5\,\pi\right)\cos\theta_A + \left(1 - x^{'}\right)\sin\theta_A}{\left(L^{'2} + l^{'2}\right) + 0.25\pi^2 - L^{'}(\pi - 2l^{'}) - \pi l^{'} + \left(1 - x^{'}\right)^2}, \frac{\pi}{2} \le l^{'} \le \frac{\pi}{2} + \frac{1}{4}, \quad \text{(S4b)}$$

$$\frac{P_b}{2\sigma}r = \frac{\left(4 + L^{'}\right)\cos\theta_A - \cos\left(0.25 - l^{'} - \theta_A\right) - x^{'}\sin\theta_A}{17 + 8L^{'} + L^{'2} + x^{'2} - \left(8 + 2L^{'}\right)\cos\left(0.25 - l^{'}\right) + 2x^{'}\sin\left(0.25 - l^{'}\right)}, \frac{\pi}{2} + \frac{1}{4} \le l^{'} \le \pi + \frac{1}{4}, \quad \text{(S4c)}$$

Considering the equal intrinsic contact angle on both sides of the air-fluid interface (Figure S7(e)), $x^{'}$ is related to $l^{'}$ through the following equation at the 1st segment:

$$\alpha = \frac{\pi - l^{'}}{2} \tag{S5a-1}$$

$$x = r\sin l^{'} + \frac{L - r\cos l^{'}}{\tan\frac{\pi - l^{'}}{2}} \tag{S5a-2}$$

$$x^{'} = \sin l^{'} + 2\tan\frac{l^{'}}{2} - \cos l^{'}\tan\frac{l^{'}}{2} = 3\tan\frac{l^{'}}{2}, 0 \le l^{'} \le \frac{\pi}{2}. \tag{S5a-3}$$

The air-liquid interface appears in a motion of translation at the 2nd segment:

$$x^{'} = 3 + l^{'} - \frac{\pi}{2}, \frac{\pi}{2} < l^{'} \le \frac{\pi}{2} + \frac{1}{4}. \tag{S5b}$$

The 3rd segment is similar to the 1st segment:

$$\alpha = \frac{\pi - (l^{'} - \frac{1}{4})}{2} \tag{S5c-1}$$

$$x = r\sin(l^{'} - \frac{1}{4}) + \frac{L + \frac{r}{4} - r\cos(l^{'} - \frac{1}{4})}{\tan\frac{\pi - (l^{'} - \frac{1}{4})}{2}} \tag{S5c-2}$$

$$x^{'} = \sin(l^{'} - \frac{1}{4}) + 2\tan\frac{(l^{'} - \frac{1}{4})}{2} - \cos(l^{'} - \frac{1}{4})\tan\frac{(l^{'} - \frac{1}{4})}{2} \tag{S5c-3}$$

$$x^{'} = 3.25\tan\left(\frac{l^{'}}{2} - \frac{1}{8}\right), \frac{\pi}{2} + \frac{1}{4} < l^{'} \le \pi + \frac{1}{4} \tag{S5c-4}$$

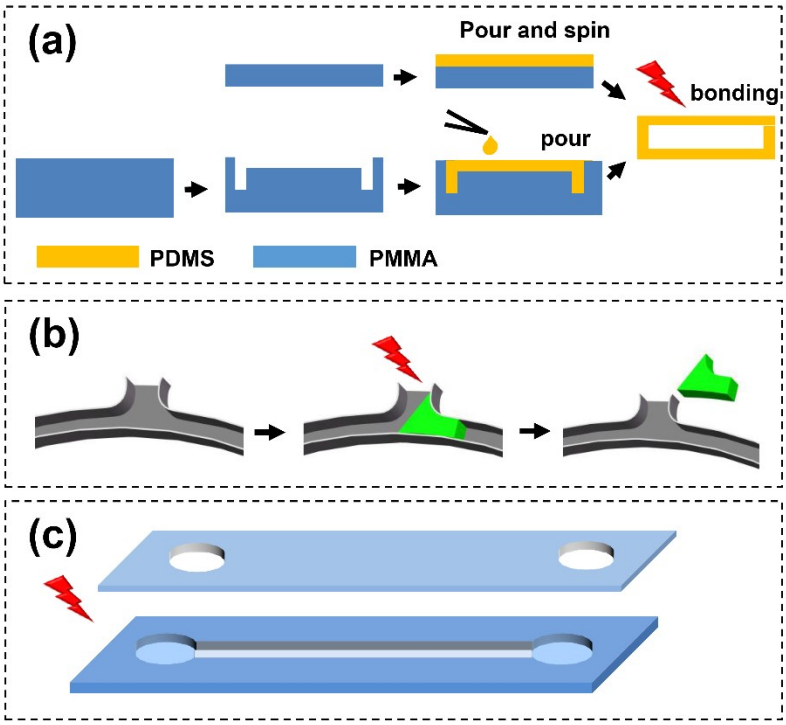

Figure S1. Fabrication procedures of microfluidic devices with one-opening chambers and hydrophobic valves (HVs), with fabrication procedures of (a) a microfluidic device, (b) a hydrophobic valve in a hydrophilic channel, and (c) a microfluidic channel.

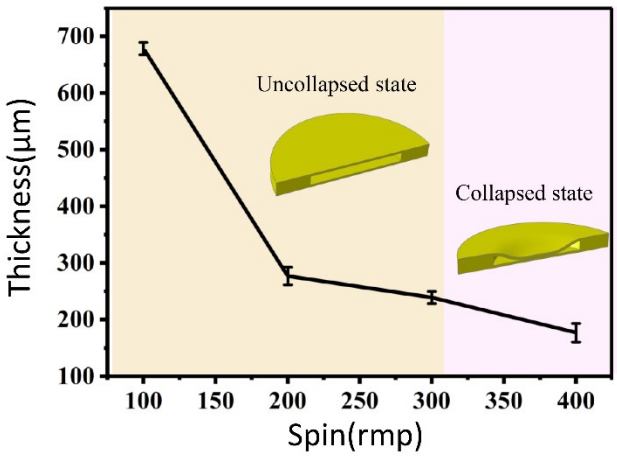

Figure S2. The dependence of the collapsed state on the thickness of the PDMS capping layer.

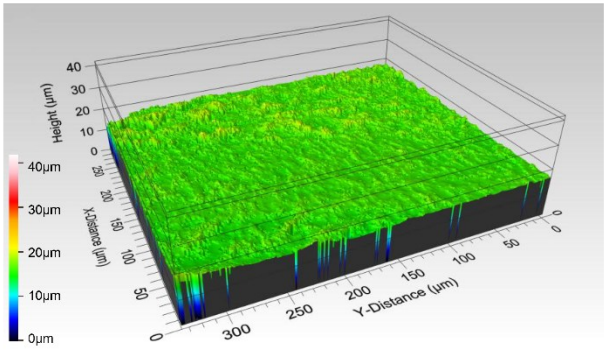

Figure S3. The surface roughness of the microchannel measured by the 3D optical profilometer.

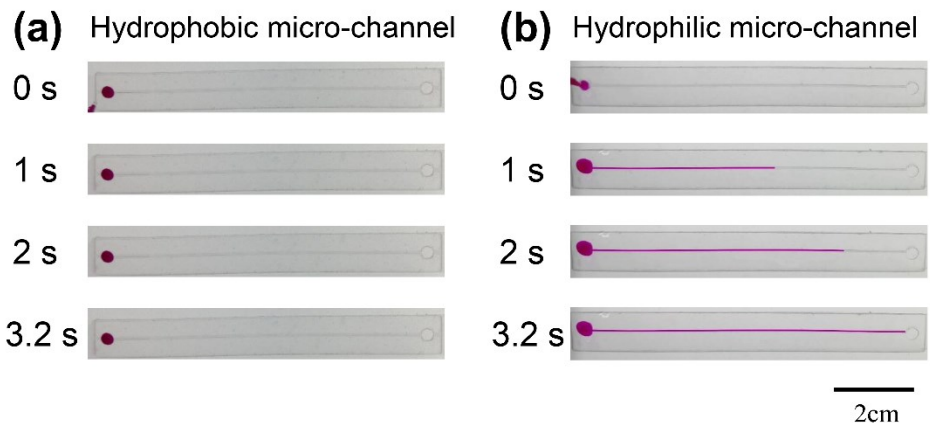

Figure S4. Sequences of photographs showing the liquid flow in (a) hydrophobic and (b) hydrophilic microfluidic channel.

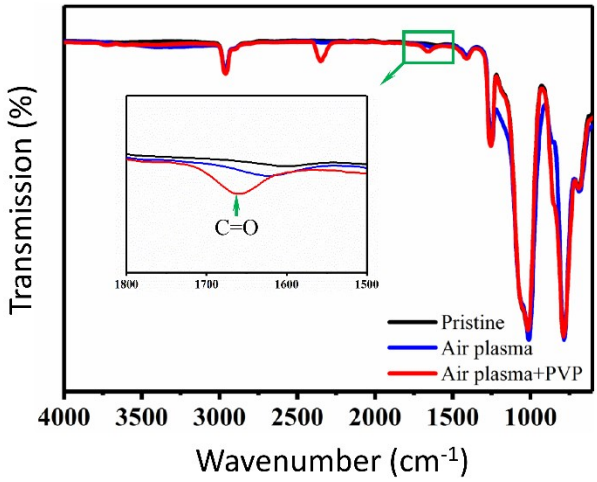

Figure S5. ATR-FTIR spectra of pristine PDMS (black), APT-treated PDMS (blue), APT-treated and PVP-modified PDMS (red).

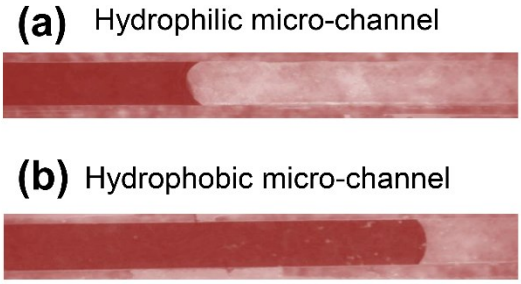

Figure S6. Optical images of the air-liquid interface in (a) hydrophilic and (b) hydrophobic microfluidic channel.

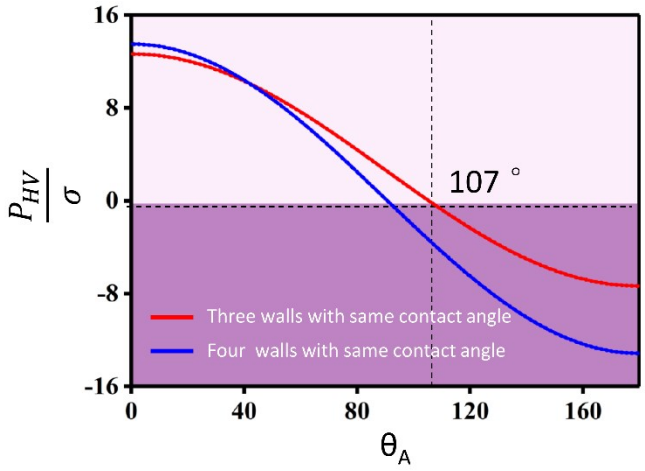

Figure S7. The impeditive function as a function of the contact angle experienced by the HV. The blue or red curve corresponds to the HV with four or three hydrophobic walls, where the hydrophilic top wall has a constant contact angle of 42°.

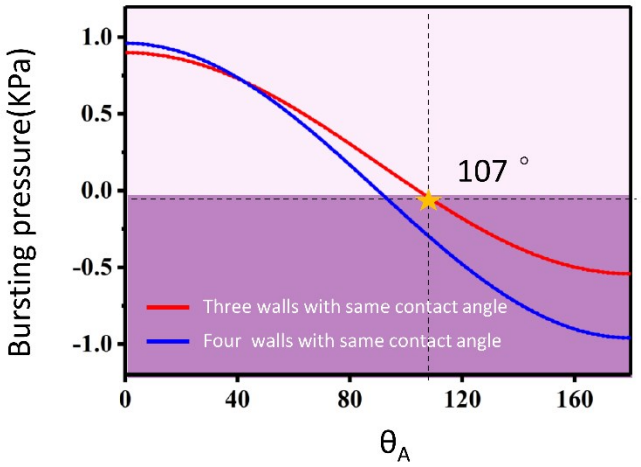

Figure S8. The bursting pressure as a function of the contact angle experienced by the HV. The blue or red curve corresponds to the HV with four or three hydrophobic walls, where the hydrophilic top wall has a constant contact angle of 42°.

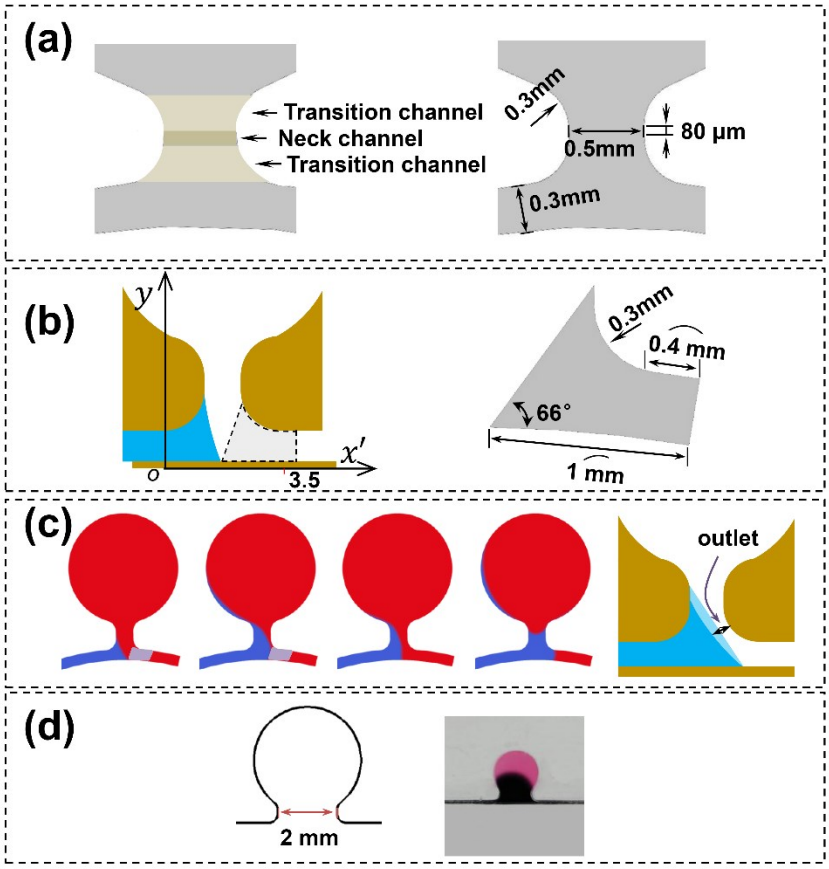

Figure S9. Design of (a) the bridging channel and (b) the hydrophobic valve. (c) Numerical simulation of the hydrodynamic flow process to the one-opening chamber with a hydrophobic valve and a longer neck microchannel (i.e., length of 200 μm). (d) Optical image highlighting the significant diffusion between two different fluids in the chamber with a wider neck microchannel (i.e., width of 2 mm).

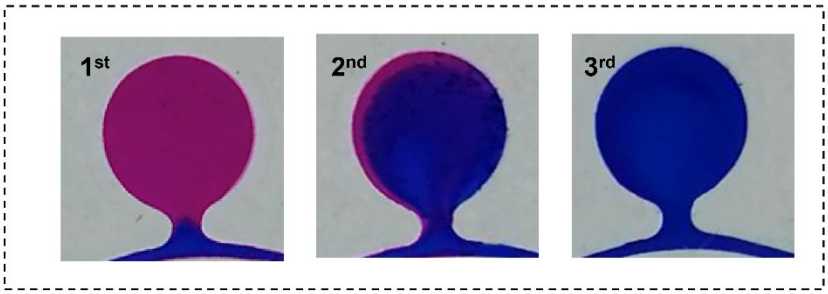

Figure S10. Optical images of two different fluids in three chambers: 1st fluid in the 1st chamber and the 2nd fluid in the 3rd chamber with 5% mixing in the total volume of each chamber.

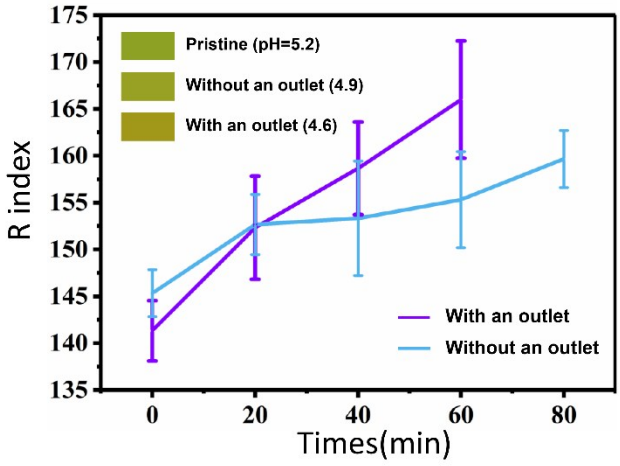

Figure S11. The change of R index as a function of time in two different chamber designs (i.e., with and without the 0.45 mm outlet).

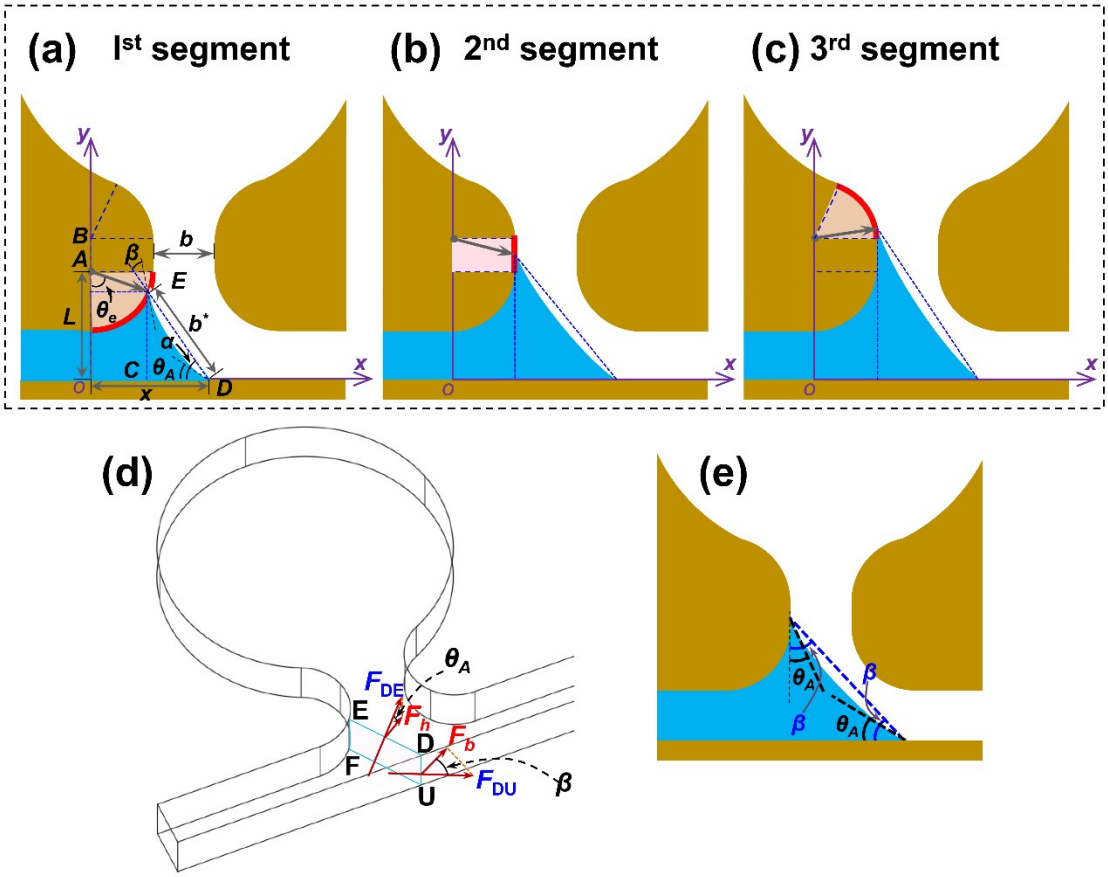

Figure S12. Schematic of the fluid front in the one-opening chambers with the HV, with the advancing front of the air-fluid interface located in the (a) bottom transition channel, (b) short microchannel, and (c) the top transition channel. (d) The two perpendicular components of the surface tension to the liquid surface. (e) The equal intrinsic contact angle on both sides of the air-fluid interface.

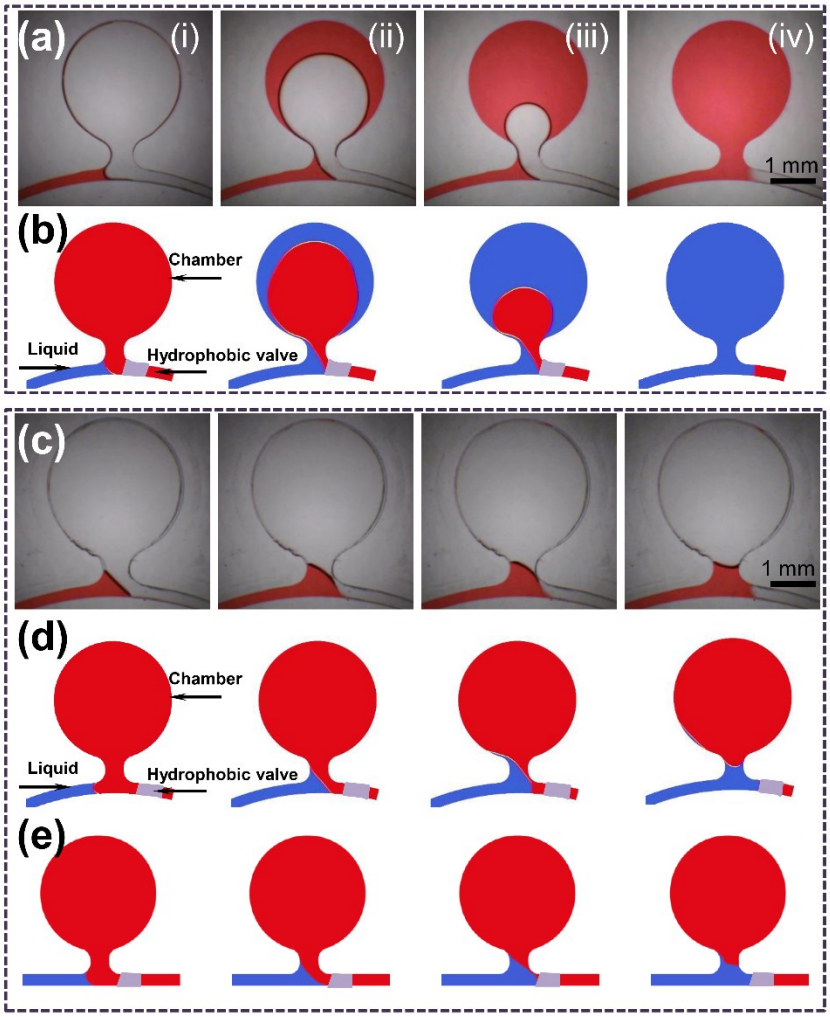

Figure S13. The hydrodynamic flow process of a unit cell with a hydrophobic valve at different positions: (a) experimental and (b) simulated results for x = 0.82 mm ($x_c^{'} = 2.7$); (c) experimental and (d-e) simulated results with a (d) rounded and (e) straight main microfluidic channel for x = 1.1 mm ($x_c^{'} = 3.6$).